Lorentz Force Control of Turbulence

by

Kenneth Breuer

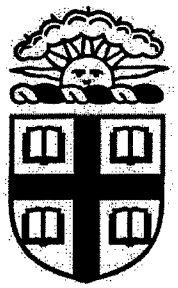

MFL TR 2005-1

Microfluidics Laboratory
Division of Engineering
Brown University

Providence, RI 02912

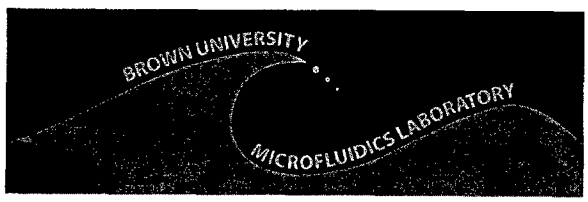

Jan 2005

REPORT DOCUMENTATION PAGE

Form Approved
OMB No. 0704-0188

1. REPORT DATE *(DD-MM-YYYY)*	2. REPORT TYPE	3. DATES COVERED *(From - To)*
4/8/05	Final Technical Report	9/30/02-5/31/04

4. TITLE AND SUBTITLE
Lorentz Force Control of Turbulence

5a. CONTRACT NUMBER
n/a

5b. GRANT NUMBER
N00014-02-1-1057

5c. PROGRAM ELEMENT NUMBER
n/a

6. AUTHOR(S)
Breuer, Kenneth

5d. PROJECT NUMBER
n/a

5e. TASK NUMBER
n/a

5f. WORK UNIT NUMBER
n/a

7. PERFORMING ORGANIZATION NAME(S) AND ADDRESS(ES)
Brown University
Division of Engineering
Box D, Providence, RI 02912

8. PERFORMING ORGANIZATION REPORT NUMBER
n/a

9. SPONSORING/MONITORING AGENCY NAME(S) AND ADDRESS(ES)
Office of Naval Research
495 Summer Street, Room 627
Boston, MA 02210-2109

10. SPONSOR/MONITOR'S ACRONYM(S)
ONR

11. SPONSOR/MONITOR'S REPORT NUMBER(S)
n/a

12. DISTRIBUTION/AVAILABILITY STATEMENT
Approved for Public Release; distribution is Unlimited

13. SUPPLEMENTARY NOTES

14. ABSTRACT
Lorentz Force actuators were developed and characterized. They were used to measure the effect of lorentz force control on the drag of a fully turbulent channel flow. Approximately 15% drag reduction was achieved

15. SUBJECT TERMS
Turbulence Flow Control, Lorentz Force, Electrohydrodynamics

16. SECURITY CLASSIFICATION OF:			17. LIMITATION OF ABSTRACT	18. NUMBER OF PAGES	19a. NAME OF RESPONSIBLE PERSON
a. REPORT	b. ABSTRACT	c. THIS PAGE			Kenneth Breuer
					19b. TELEPHONE NUMBER *(Include area code)* 401-863-2870

This report is the final technical report for the ONR award (Brown Account 5-25020) that expired on 5/31/2004. Any technical questions should be addressed to *kbreuer@brown.edu*

Contents

List of Tables

List of Figures

Chapter 1

Introduction

1.1 Background

Improved understanding of unsteady flow physics has led to a wealth of flow control applications in which fluid perturbations are deliberately introduced into a large-scale flow with the goal of affecting its global characteristics. Research into these methods has included separation control, enhanced mixing, and reduction of turbulent skin friction. Interest in turbulence control has grown due to numerical computations at low Reynolds number flow [3, 4, 5] which indicate that the turbulence and drag can be reduced by a variety of fluidic actuations. The difficulty with these methods is that even though computationally they provide promising results, implementing them in a physical experiment proves very difficult. Other actuation methods that have been studied experimentally include localized heating [6], piezo-electric flaps [7], oscillatory blowing [8], synthetic jets [9], surface motion [10] and plasma discharge [11].

Given the previous problems with designing robust actuators, an appealing approach for turbulence suppression in an electrically conducting fluid is Lorentz force actuation. Lorentz force actuators have no moving parts and thus in principle are easy to implement. When a current, I, and a magnetic field, B, interact, the Lorentz body force, F_L, is generated:

$$F_L = IB\ a \tag{1.1}$$

where a is the characteristic length over which the current flows. The motivation for this application comes from the recognition that an oscillatory wall motion disrupts the spanwise structure of the equilibrium turbulent flow, disturbing the turbulence production cycle and consequently the turbulent drag [5, 12].

Recent experimental results have been published by Di Cicca et al. [13] and Pang and Choi [14] documenting reductions in shear at the wall using oscillatory wall motion and Lorentz force actuators, respectively. Di Cicca et al. documented particle image velocimetry measurements of a turbulent boundary layer with an oscillating wall. Experiments were conducted in a closed loop open surface water channel, with the wall oscillating at a frequency of $T^+ = 100$ (2.67 Hz) and a peak to peak amplitude of 2 cm. Results showed that turbulent velocity fluctuations were considerably reduced, while the PIV allowed measurements of the physical mechanisms taking place in the boundary layer. The main result of these

experiments was that the mean velocity increased with actuation, and was accompanied by a decrease in turbulence production.

Pang and Choi [14] recently published experiments conducted in an open surface water channel using Lorentz force actuation. Actuators cover an area $\approx$ 300 mm x 230 mm where a high conductivity solution ($CuSO_4$) was injected at the surface to create an electrically conductive environment. The maximum velocity in the mean profile was found to have increased approximately 66% with actuation, when u^+ was nondimensionalized using its own friction velocity (u_τ).

1.2 Review of scaling arguments

A scaling argument was developed by Breuer, Park and Henoch [1] for which a brief review will be presented here. In Lorentz forcing, in order for the control to be effective, the force must be able to induce a spanwise velocity in the fluid of approximately u_τ. The Stuart number, St, is defined as the ratio of the Lorentz inertia, JBa, to the fluid inertia, ρu_τ^2, and should be approximately equal to 1. The current density, J, is defined as the total current divided by the total wetted area. Thus an expression can be obtained for the optimal Stuart number at which Lorentz forcing will be effective:

$$St = \frac{JBa}{\rho u_\tau^2}. \tag{1.2}$$

Defining a and T in terms of turbulent wall units: $a = a^+\nu/u_\tau; T = T^+\nu/u_\tau^2$ allows us to redefine the optimal Stuart number as

$$St = \frac{a}{u_\tau T} = \frac{a^+}{T^+}. \tag{1.3}$$

We can extend this scaling argument slightly further for the current experiments, in which the electrode spacing a has a fixed size, but is nevertheless used in flows with different Reynolds numbers. Thus its "apparent" size, a^+, increases as the Reynolds number of the flow increases. It is trivial to re-write the definition of the Stuart number (1.3) as

$$St = \frac{a}{h}\frac{Re^*}{T^+} \tag{1.4}$$

where h is the channel half-height and Re^* is the turbulent Reynolds number: $Re^* = u_\tau h/\nu$. Thus we see that, for a fixed value of a, we predict that the optimal value of the period will also rise linearly with Reynolds number, and that for a fixed non-dimensional period, the optimal Stuart number will also scale with Re^*. This gives a dimensionless parameter T^+St/Re^* that for optimum forcing remains constant, regardless of flow rate. The experimental data confirms these predictions both for the drag reduction experiments performed by Breuer, et al. [1] as well as the flow measurements reported here.

1.3 Current Experiments

Experiments reported by Breuer et al. [1] provided a basis for the research presented here. In these experiments, Lorentz force actuators were assembled together to form a large plate from which direct drag measurements were obtained. The actuator was designed for robustness in the harsh saltwater environment. The electrodes were tested extensively for effectiveness, and a polymer coating was found to decrease both electrolytic effects during actuation as well as corrosion effects. Spanwise oscillation as well as travelling wave actuation were tested. Testing was somewhat limited, as corrosion and degradation of the actuators limited experiment duration. Because of this, design changes were made and implemented in the actuator fabrication to help prevent corrosion and increase experimental longevity. The experimental procedure and apparatus was also changed to achieve more accurate results in the near wall region. The drag measurements did not include flow data, so PIV was implemented to obtain velocity fields. The range of forcing parameters was expanded, as well as sampling from a broader range of Reynolds numbers. In addition to providing flow visualization, the data further confirms the scaling arguments presented for optimum Lorentz force control. Experiments were run to study the effects of different phases of the forcing cycle, and data analysis was expanded to include integrated actuation data for both low and high Reynolds numbers, R_{uu} and R_{uv} two point correlations, and conditional averaging.

Chapter 2

Experimental Setup and Procedure

2.1 Actuator Design and Fabrication

The actuator design is based on the actuator developed and tested by Henoch and Stace [15] and Breuer et al. [1] which used arrays of magnets and electrodes to generate a uniform Lorentz force acting in the streamwise direction (figure 2.1). The actuator used in the current experiments rotates the Henoch and Stace design 90 degrees, so the Lorentz force now acts in the spanwise direction, perpendicular to the core flow. Linear arrays of permanent magnets are interlaced with a commercially fabricated printed circuit board to generate the necessary fields.

The segmentation of the electrodes in the spanwise direction allows multiple forcing regimens. Spanwise oscillation, simulated by Berger et al. [16], can be achieved by actuating all of the spanwise columns in unison (i.e. with zero phase shift). Operating the electrodes with the same amplitude and time-signal but including a spanwise phase shift generates a travelling wave, explored computationally by Du and Karniadakis [17]. They found that actuation via a transverse travelling wave eliminated near-wall streaks, reducing shear stress by more than 30%. The current experiments explore spanwise oscillation only, although the circuit boards have the capacity to utilize 16 independent channels, making travelling wave actuation a possibility.

Based on the experiments run by Breuer et al. [1] some design modifications have been made. Previously, the magnets were aligned on the flux plate using stainless steel pins. The installation of these pins was both difficult and time-consuming. To improve fabrication time as well as reduce corrosion, plastic dowel pins were substituted. After removal of the actuators from the previous experiments, it was found that the tiles were most susceptible to saltwater penetration through the side walls. To help prevent this in future experiments, a 1/8" epoxy border was created on all sides of the actuator (excluding the top surface). The Nd-Bo-Fe permanent magnets used were also found to have suffered corrosion damage, due to a non-uniform epoxy coating. New magnets were obtained, which were both nickel plated and epoxy coated to help maintain their integrity throughout the course of the experiments.

Fabrication of the actuators was a time-consuming, multi-step process. The base of the fixture is a 12" $\times$12" $\times$1/8" low carbon steel plate. The plates met a flatness spec of 0.008" in all directions. Low carbon steel was chosen for its machinability, as over eight hundred holes

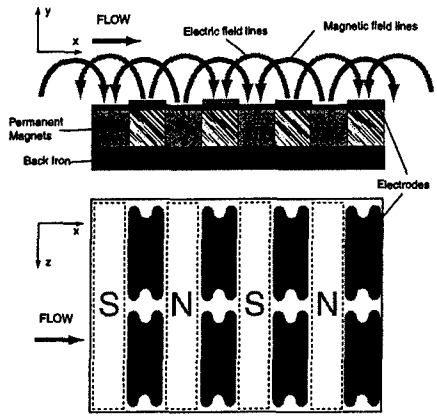

Figure 2.1: Schematic of the Lorentz Force Actuator showing side and top views respectively. The Lorentz force acts in the spanwise direction, out of the page on the side view and from top to bottom on the top view [1].

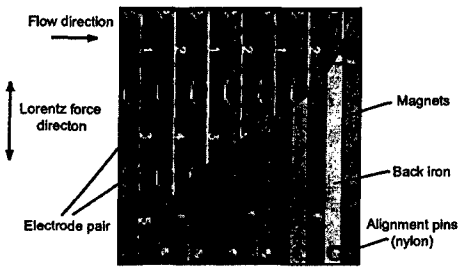

Figure 2.2: Composite photograph of Lorentz-force actuator showing the sub-structure (flux plate, alignment pins and magnets) and the electrode layer [1]. The flow in this picture is from left to right, and the Lorentz force is from top to bottom. The streamwise pitch of the magnets and electrodes is 3.125mm.

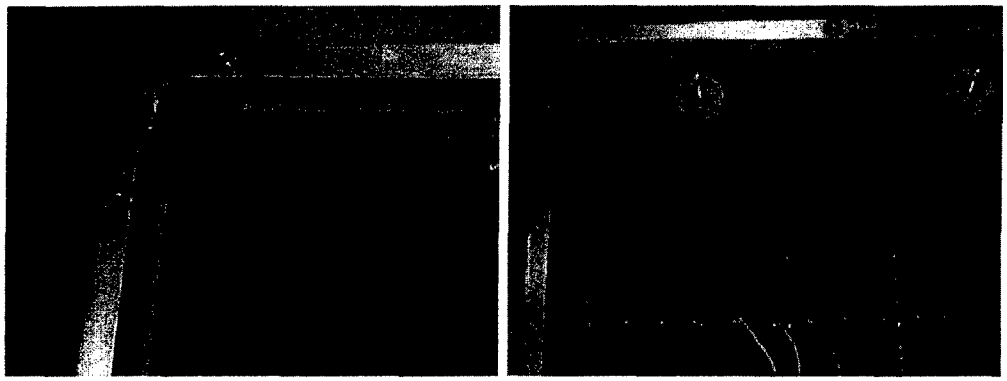

Figure 2.3: Photographs showing (a) PCB in aluminum mold with tape border and 1/8" spacer inserted into corner and (b) finished plate with epoxy coating and "levelling feet" embedded on the back surface. Holes drilled through the flux plate to allow seepage are also visible.

were required for alignment pins, epoxy seepage, and structural attachment. Neodymium-Boron-Iron (45 M-O) permanent magnets (Adams Magnetics, Elizabethtown KY) were dual coated with nickel and epoxy to help prevent degradation in the harsh saltwater environment. The magnets have a 1/8" square cross section and a length of 2". Longer lengths would have made assembly much easier; however, the strength of the magnetic field as well as the brittleness of the magnets were limiting factors. The magnets were aligned in rows in the spanwise direction using plastic dowel pins. These 3/32" diameter, 1/8" long pins were inserted individually into the plate in pre-drilled holes, making the assembly very tedious. The magnets were then attached to the plate and maneuvered into place against the plastic pins, giving a very precise array. A composite photograph containing both the magnet-pin structure as well as the electrode layer is shown in figure 2.2.

The electrode layer consists of a commercially fabricated two-layer printed circuit board (Multi-Lab, Inc. Manchester, MA). The electrodes protrude slightly above the surface, but are hydrodynamically smooth (step less than 1l^*). To increase the effective electrode separation the electrodes are designed with a "cut back" between spanwise columns. The surface of the circuit board was screen printed with a polymer ink to both reduce the electrolytic effects during actuation and prevent corrosion. Thirty-two wires were soldered to each board with a length of 21 feet so that each wire could be directly connected to the amplifiers, alleviating the need for cumbersome bus lines.

A mold was designed (figure 2.3) to facilitate the assembly of the magnet/flux plate fixture to the circuit board. The inner dimensions of the Aluminum mold were machined to be 12 1/4" square, to allow for the epoxy border around the outside. The walls of the mold are detachable, giving easy removal after the epoxy has cured. To maintain a constant mold size, a plastic template precision machined to the correct dimensions was used to size the mold before each use. All of the inner surfaces were then coated with a silicone spray, to prevent sticking and subsequent cracking of the epoxy upon removal. The top (actuated) surface of the PCB was covered with a sheet of plastic and masking tape to prevent seepage of epoxy onto the electrodes. A 1/8" border of masking tape was allowed on the outside of

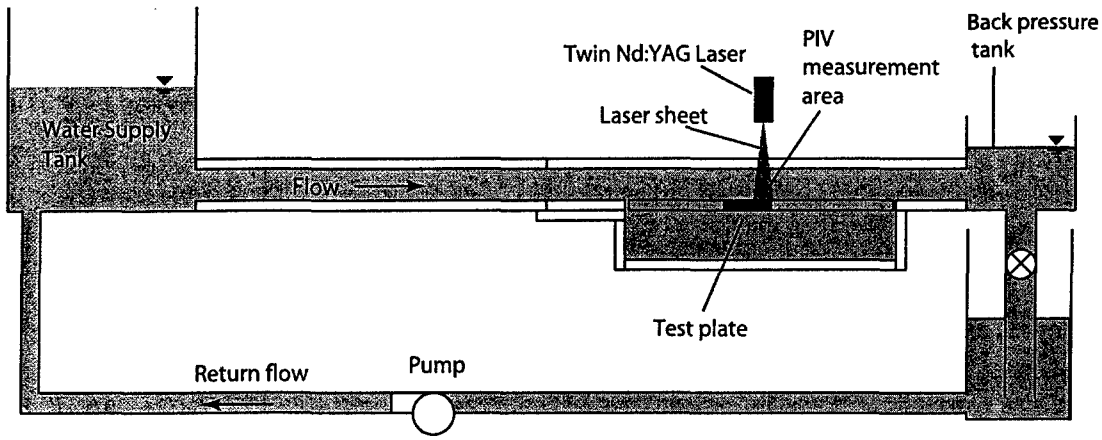

Figure 2.4: Schematic of flow facility, showing the back pressure and water supply tanks, development section, test area with actuator and return flow path.

the circuit board to center it in the mold. Levelling feet were attached to the bottom surface of the steel plate using brass set screws. These 1" diameter, 1/2" thick polypropylene discs were used to assure flatness of the plates when installed into the channel, as well as aiding in the removal of the plates from the mold. The magnet/flux plate fixture was suspended above the mold containing the circuit board while the wires were individually fed through the assigned holes.

The PCB was attached to the magnet/flux plate fixture using a commercially available epoxy (Emerson and Cuming Stycast 2057 black epoxy), chosen because it is waterproof and corrosion resistant. Once the circuit board was mounted in the mold and the wires were fed through the steel base plate, the epoxy was mixed continuously with the hardener for two minutes to ensure continuity. The mixture was poured over the PCB, and the flux plate was lowered in increments to make sure none of the wires were crimped and subsequently damaged when the actuator was clamped. To make sure the actuator plate was centered in the mold, four 90 degree 1/8" L-bracket spacers were placed in the corners. The spacers were removed only after the plate was completely lowered into the mold and clamps applied holding the levelling feet firmly to the mold. The remainder of the epoxy mixture was poured and evened, and was given a full 24 hours to cure. After complete hardening the mold was carefully removed piece by piece to avoid cracking the plate, and all actuators were checked for continuity.

2.2 Flow Facility

The flow facility (figure 2.4) at Brown University is a constant pressure channel that can support both saltwater and freshwater experiments, with flow rates between $Re^* = 100$ and $Re^* = 800$. The entire channel is constructed of clear acrylic for ease of PIV measurement as well as corrosion resistance and is built on 80-20 supports. Flow is pumped from the

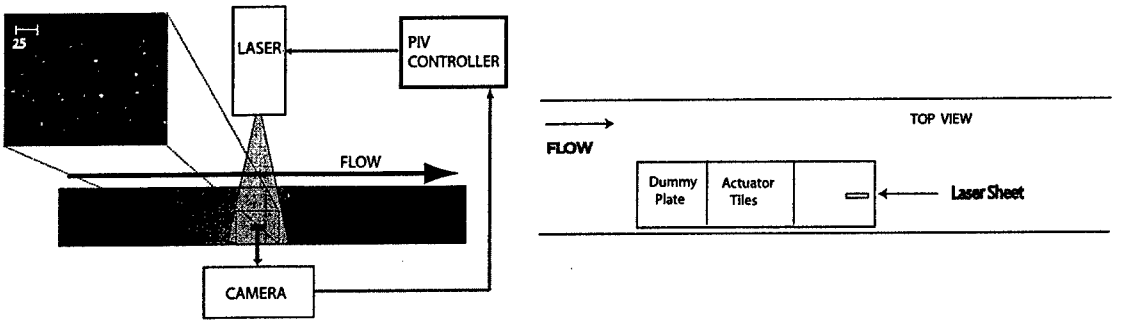

Figure 2.5: Schematic showing side and top views of PIV setup. A laser sheet in the x-y plane is produced by an Nd:YAG laser mounted above the channel. The image size is approximately 9×11mm.

Parameter	Flow Rate 1	Flow Rate 2	Flow Rate 3	Flow Rate 4
u_τ[m/s]	0.0064	0.0087	0.0132	0.0147
t^* [ms]	26.0	13.5	5.7	4.5
l^* [μ m]	166.10	117.9	74.9	67.5
Re^*	144	167	305	330
Frequencies [Hz]	(0.3 - 3.2)	(0.2 - 4.1)	(0.3 - 1.6)	(0.8 - 4.1)
Amplitudes [V_{0-p}]	(0.5 - 3.5)	(1.5 - 4.5)	(3.0 - 5.0)	(2.0 - 5.5)
St	(2.9 -19.0)	(7.0 - 17.9)	(3.5 - 6.8)	(2.2 - 5.7)
T^+	(12 - 123)	(13 - 265)	(104 - 564)	(52 - 258)

Table 2.1: Forcing frequencies, amplitudes, dimensionless numbers and flow parameters for the four flow rates used.

collection tank through a series of four pumps up to the accumulation tank. Flow then continues into the development section through a honeycomb and over a strip of velcro that forces early transition to turbulence. The development section is 3m long, 1m wide, and 24mm high. The flow then enters the specially designed test section.

The floor of the test section is a removable table that allows installation and adjustment of multiple actuators. Snorkels in the roof of the channel as well as a "fence" along the side of the test section permit the wires to be fed out of the channel to the amplifiers without disturbing the main flow. Portholes in the roof give easy access for calibration and cleaning. Salt was added to a mass concentration of 3.5% giving a conductivity of 4.5 Siemens/m, closely matching that of seawater. The channel was then run for eight hours to provide adequate time for mixing.

Numerous control and monitoring devices have been installed for precise control and repeatability of experiments. It was found that the temperature increase due to work added to the system by the pumps was approximately three degrees per hour, significantly changing the viscosity. A heat exchanger (NESLAB HX-150DD) was used in the collection tank to reduce the temperature variation to within 0.2 degrees over a three hour experiment. A valve system allows flow to bypass the main channel, giving more precise control of flow rate. The flow rate was continually monitored during testing using a fixed-depth turbine flow sensor

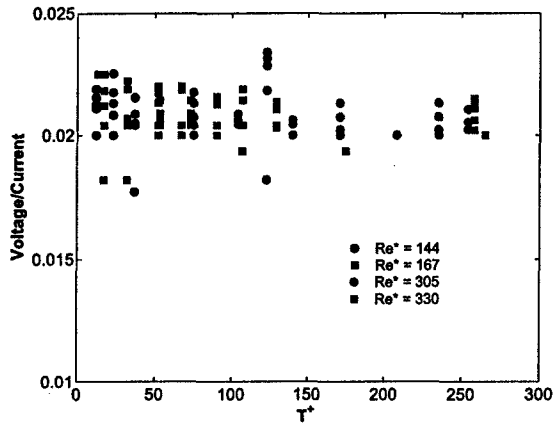

Figure 2.6: Experimentally measured voltage divided by current plotted with actuation frequency (T^+). V/I remains approximately constant for all experiments.

(Seametrics).

Trapped air under the plates caused bubbles during PIV measurements, decreasing the clarity of the image. The surface of the actuator tiles was cleaned before each experiment and a specially designed wiper allowed for "sweeping" of the test surface as well as the roof of the channel during testing. The temperature, flow rate and pressure head were monitored and recorded during each actuation. Sinusoidal waveforms were produced using a Stanford Research Systems Waveform Generator and a 16-channel custom built amplifier. Power is supplied by 2-10V power supplies (Lambda), and current to the actuators was continuously monitored using an open loop current sensor (Sypris, IHA-25). Figure 2.6 shows the experimentally measured voltage divided by current plotted with the forcing period, T^+. As expected, the value remains constant for all experiments.

2.3 Particle Image Velocimetry System

A Particle Image Velocimetry (PIV) System was used to obtain velocity data. Pairs of images were acquired from which full velocity fields were calculated. A schematic showing the PIV setup is presented in figure 2.5. A 15 mW Nd:YAG laser is mounted on a traverse which moves in the spanwise direction, with attached optics that create a laser sheet in the $x-y$ plane. The laser and the camera can be moved such that measurements can also be taken in the $x-z$ plane. A 3D precision stage with micrometer adjustment capabilities holds the camera and allows for fine corrections during testing. An Infinity lens (InFocus Model KC) which has both a large working distance ($\approx$ 350mm) as well as a large field of view allowed magnified images near the wall. PIV software (IDT proVISION, release 2.01) was used to process the images after acquisition. Image calibration was achieved using a 1" Aluminum block drilled with holes in a 2mm square grid. The laser sheet was located approximately 2cm upstream from the end of the actuator plates, and was centered on the actuator in the spanwise direction.

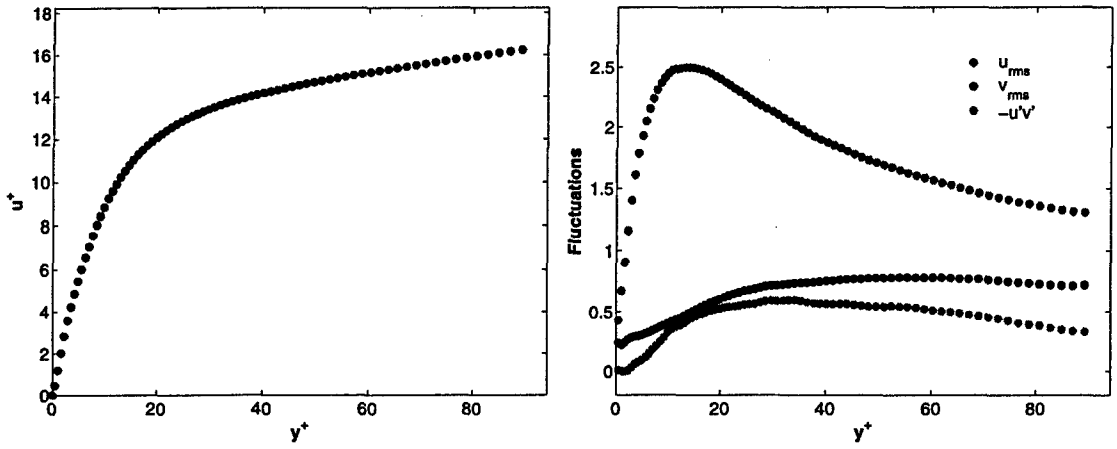

Figure 2.7: PIV baseline channel velocity profiles showing both mean flow and fluctuations. Profiles demonstrate fully developed turbulent flow at $Re^* = 167$. All quantities are normalized by the friction velocity, u_τ.

2.4 Experimental Procedure

Before each data acquisition, the setup was allowed to run for approximately 30 minutes. This allowed the flow rate to become constant as well as any bubbles to be flushed out of the channel. Bubbles on the actuated surface scattered the laser light and blurred the image, and proved difficult to get rid of. The roof of the channel also gathered bubbles easily, distorting the laser sheet. A specially designed 'bubble scraper' allowed the surfaces to be cleaned during testing. This allowed the integrity of the image to be maintained through the course of the experiment, without altering the flow rate or pressure head.

After the system was allowed to come to equilibrium, an initial baseline case was taken. The data was immediately processed using the PIV software to assure accurate results. Barring any abnormalities in the flow, the test matrix was then run. In between each case, the channel was given 30 seconds to allow the new forcing scheme to propagate through the entire length of the test section. Baseline cases were taken throughout the course of the experiment to ensure no drifting occurred.

In early experiments, glare from the electrodes made obtaining accurate near wall data difficult. By adjusting the contrast and laser intensity, consistent measurements were made to $y^+ \approx 4$. A smaller mesh size and corresponding interrogation area were used close to the wall, allowing a more accurate correlation. The 1360×1024 pixel image was covered with a mesh that created a velocity field with approximately 50×75 vectors. The camera was rotated 90 degrees to allow the longer dimension to be perpendicular to the wall. The typical PIV interrogation area used was 36 pixels. Time separation between the laser pulses for the lower Reynolds number was $300\mu s$, compared to $150\mu s$ for the higher velocity flow. Each point in the velocity profile was obtained by averaging over approximately 50 vectors in the x-direction and 200 ensemble images.

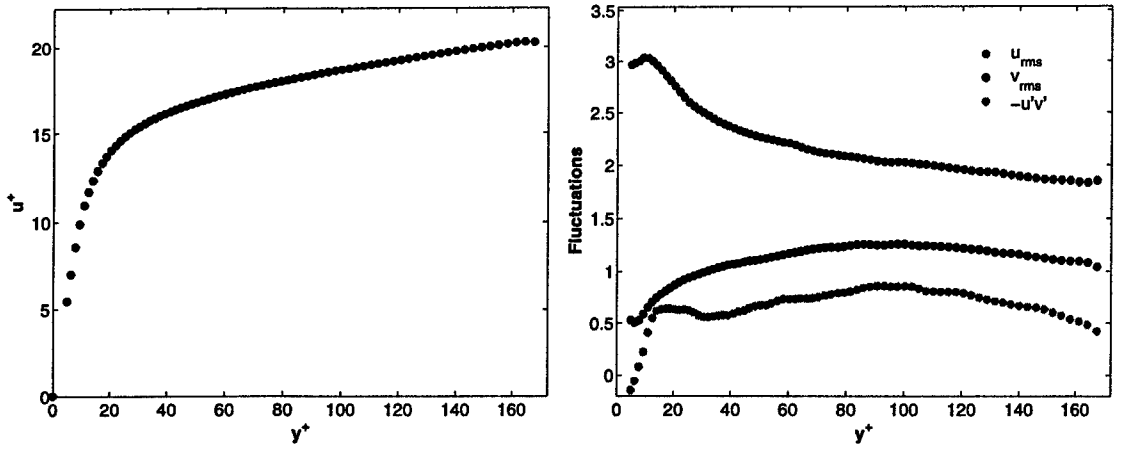

Figure 2.8: Velocity profiles at a higher Reynolds number ($Re^* = 330$) showing both the mean flow as well as the fluctuating components.

Chapter 3

Results and Discussion

3.1 Mean Flow

A series of experiments were run at two different Reynolds numbers. Figure 2.7 shows baseline channel velocity profiles for the lower Reynolds number, $Re^* = 167$. The mean flow is on the left with the fluctuations, u', v', and $-u'v'$ on the right, showing a well behaved and fully developed turbulent flow. With the previously mentioned adjustments to the experimental procedure, accurate measurements were made to within $y^+ = 4$. A second set of experiments was run at a higher velocity to study the effects of forcing with increased Reynolds number. Baseline profiles are presented in figure 2.8. All baseline as well as actuated cases have been normalized by the friction velocity (u_τ) of the unactuated case. Since the water channel is driven with a constant pressure head, u_τ remains constant for all cases. Initially, u_τ was calculated using $u^+ = y^+$ in the near wall region, and this gave a rough approximation. By matching the unactuated mean profiles with turbulence statistics from a Direct Numerical Simulation (DNS) [2], u_τ was re-scaled to give a more accurate fit. The experimental data scales well with the numerical calculations, and the results are presented in figure 3.1. The close fit not only shows good agreement between numerical simulations and experimental results, but also provides a very accurate method for determining u_τ.

3.2 First Order Statistics

3.2.1 Actuation Data

Figures 3.2 through 3.5 show profiles of the mean velocity, Reynolds stress, and turbulence production terms. For each figure, either the frequency or amplitude is held constant and results are shown for a sweep through the other parameter. In all figures presented here, blue circles represent the baseline (unactuated) case. Figure 3.2 shows a frequency sweep for a fixed amplitude (4.5 V, St = 12.9) at the lower speed flow ($Re^* = 167$). The red circles show the lowest frequency, green circles the highest, and the black circles represent the frequency that was found to produce a maximum in local flow rate accompanied by a minimum in Reynolds stress. Actuated cases show both an increase in flow rate as well as a

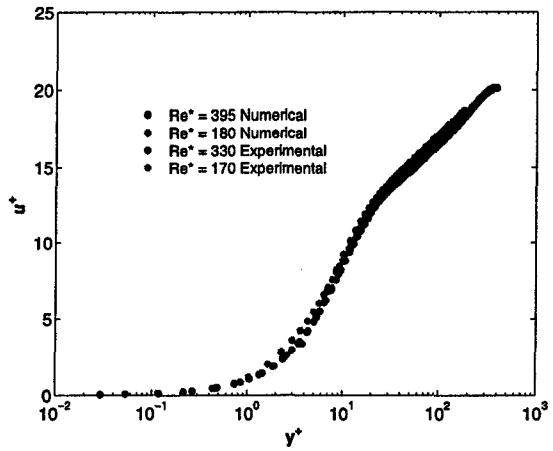

Figure 3.1: Baseline unactuated mean profiles plotted with numerical turbulence statistics for a range of Reynolds numbers from Moser et al. [2].

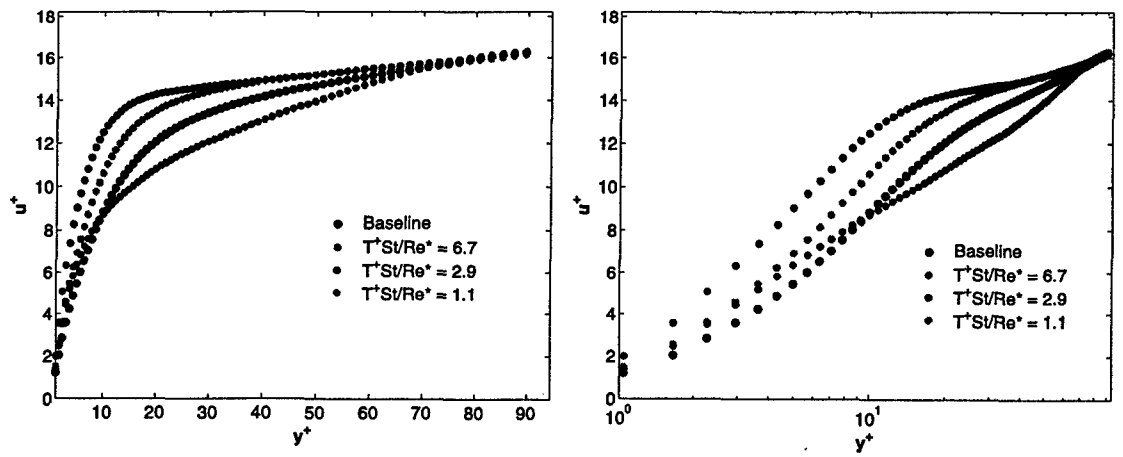

Figure 3.2: Mean flow profiles for a fixed forcing amplitude with changing frequency at $Re^* = 167$. The fixed amplitude that was chosen was the highest possible given the actuator design. Actuation both increases and decreases the fluctuations, with a local minimum around $T^+St/Re^* = 2.9$.

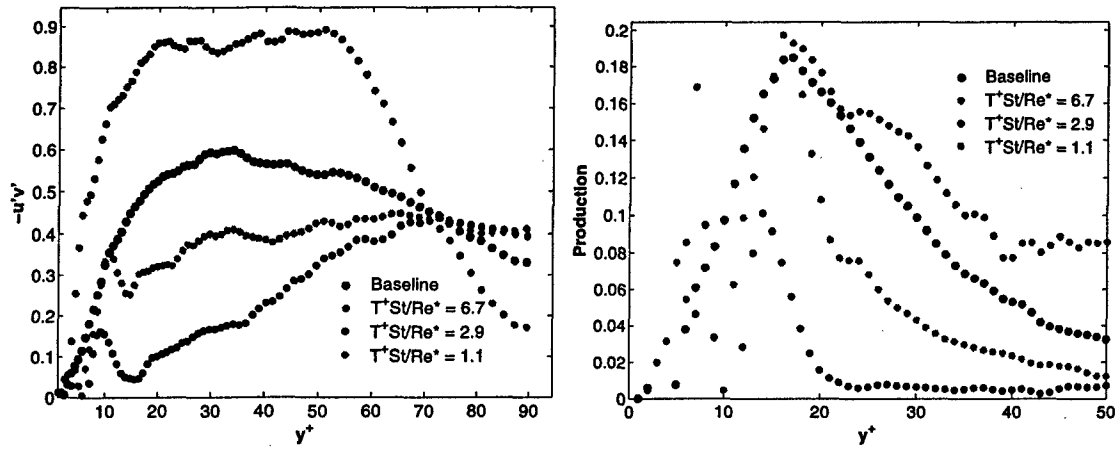

Figure 3.3: Changes in Reynolds stress and turbulence production for a constant amplitude and changing frequencies. The lowest production accompanies the highest local flow rate as well as the greatest reduction in shear stress.

decrease in Reynolds stress, demonstrating that the Lorentz forcing is indeed affecting the near wall flow.

Given the profiles for the mean flow and Reynolds stress, we can calculate the turbulence production term. Taken from the fluctuation energy equation, the turbulence production is defined as

$$P \approx -\overline{u'v'} \cdot dU/dy \tag{3.1}$$

Figure 3.3 shows the Reynolds stress and turbulence production profiles for the cases shown above. As expected, a decrease in production accompanies an increase in the mean flow and decrease in Reynolds stress. Production is calculated to $y^+ \approx 100$ as in the mean flow and Reynolds stress cases, but is plotted here only to $y^+ = 50$ to magnify the near wall region. A 'sweet spot' at $T^+St/Re^* = 2.9$ was found, showing the greatest decrease in turbulence production accompanied by the largest increase in flow rate.

Figures 3.4 and 3.5 show the effects of forcing for a higher Reynolds number ($Re^* = 330$). The actuated cases cause a change in the flow; however, the magnitude is much lower. This can be predicted from the scaling arguments made earlier by Breuer, et al. [1]. The scaling predicts that for a constant optimum value of T^+St/Re^*, when the Reynolds number is roughly doubled the optimum forcing comes when the quantity T^+St is also doubled. Due to experimental restrictions on the amount of current that can be run through the system, it was not possible to effectively double this parameter. This being said, there is still a significant change in the Reynolds stress as well as the production term. The greatest decrease in turbulence production comes at the largest forcing amplitude which correlates to a $T^+St/Re^* \approx 2.2$. Since a minimum in production has not yet been reached, it is foreseeable that increasing the current through the system can further decrease the turbulence production and increase the mean flow.

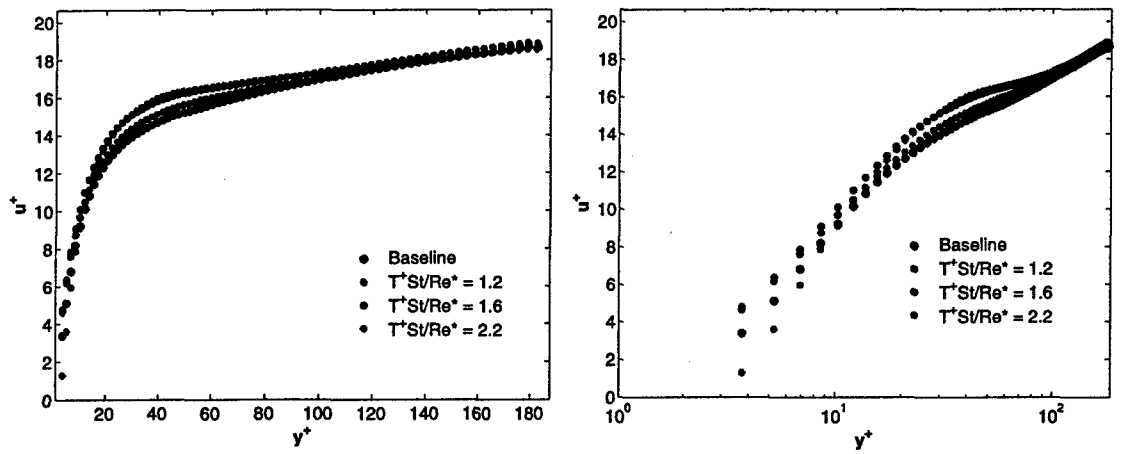

Figure 3.4: Effects of forcing on the mean flow are shown for a higher flow rate ($Re^* = 330$). One forcing frequency and three amplitudes are plotted withthe baseline.

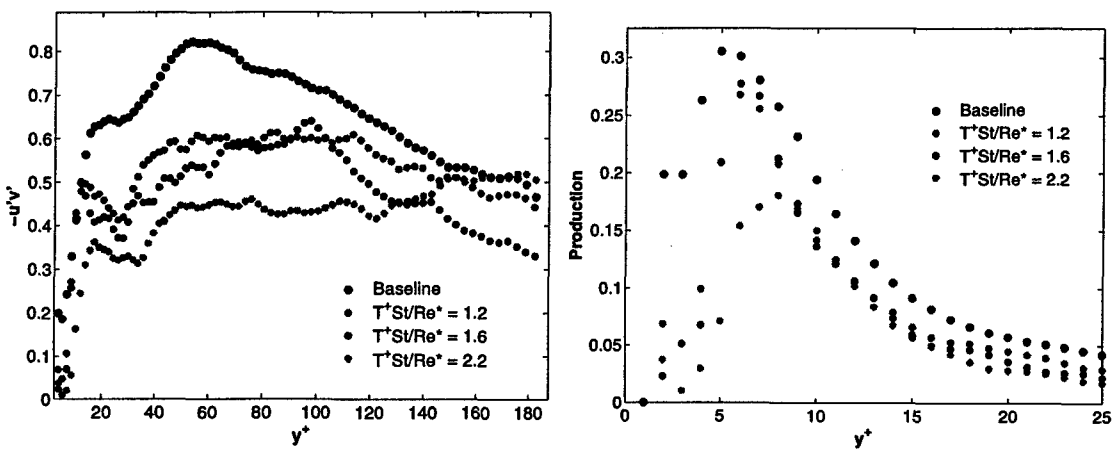

Figure 3.5: Changes in Reynolds stress and turbulence production at $Re^* = 330$. The turbulence production is greatly suppressed around the 'sweet spot' where $T^+St/Re^* = 2.2$.

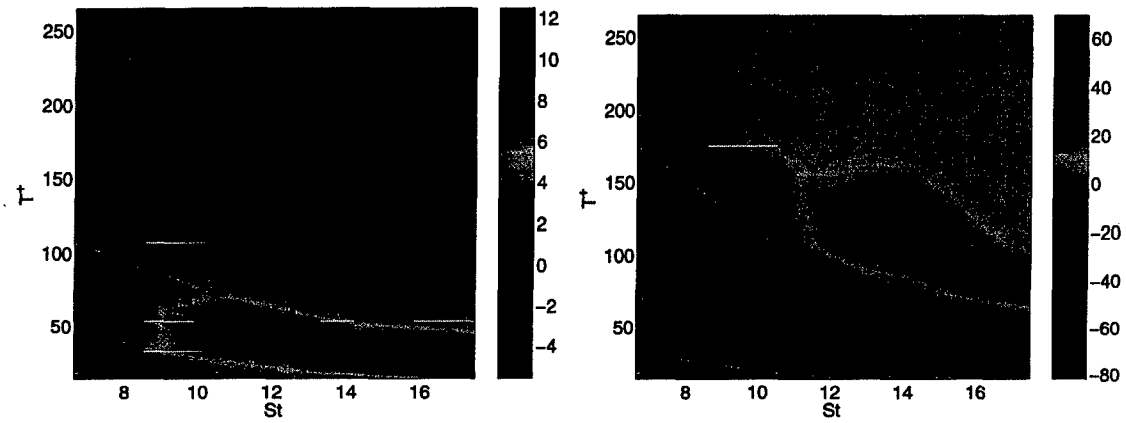

Figure 3.6: Percent change in flow rate and production terms over a wide range of forcing frequencies and amplitudes for a flow rate of $Re^* = 167$. The maximum increase in flow rate is accompanied by the greatest decrease in turbulence production, near the 'sweet spot'.

3.2.2 Integrated Flow Rate and Production

The actuated results for each Reynolds number are effectively summarized in figures 3.6 and 3.7. For each actuated case, the mean flow and production profiles were integrated to $y^+ \approx 75$ to find a local flow rate and integrated production value. The percent change from the baseline for the flow rate is shown on the left, with the accompanying change in production on the right. All forcing amplitudes are presented across the horizontal axis, spanning $St = 6.4 - 17.9$. Forcing frequencies are represented on the vertical axis, covering $T^+ = 13 - 265$. A maximum increase in flow rate, coupled with a minimum in turbulence production can be seen at $T^+ = 32$ and a $St = 17$. This correlates to a $T^+St/Re^* = 2.9$, which agrees well with the optimum conditions suggested by the mean flow and Reynolds stress plots presented earlier. It is also observed that there are regions where the flow rate decreases and the turbulence production increases, which shows that Lorentz forcing does indeed have a significant impact on the flow.

Integrated mean flow and turbulence production data for a $Re^* = 330$ is presented in figure 3.7. The flow rate increases for all actuated cases, which is expected considering there were no forcing parameters that decreased the mean flow or increased the Reynolds stress. This suggests that optimum testing conditions have not been reached. As stated previously, the actuators limit the amount of current that can be run through the system. Although all actuated cases decrease the production, the maximum change is still 20% less than for the lower Reynolds number flow, suggesting higher forcing amplitudes would be more effective.

Figure 3.8 represents all of the data taken in the current experiments, scaled by the dimensionless parameter, T^+St/Re^*. The percent change from the unactuated case for both flow rate and production are shown. Results from four separate experiments covering two ranges of Reynolds numbers are presented. Both the flow rate and turbulence production data scale well using the dimensionless ratio, and suggest an optimum forcing condition of $T^+St/Re^* \approx 2 - 3$. Lorentz forcing has less of an impact on the higher Reynolds number flow, showing a smaller change in flow rate and production. A discrepancy exists between

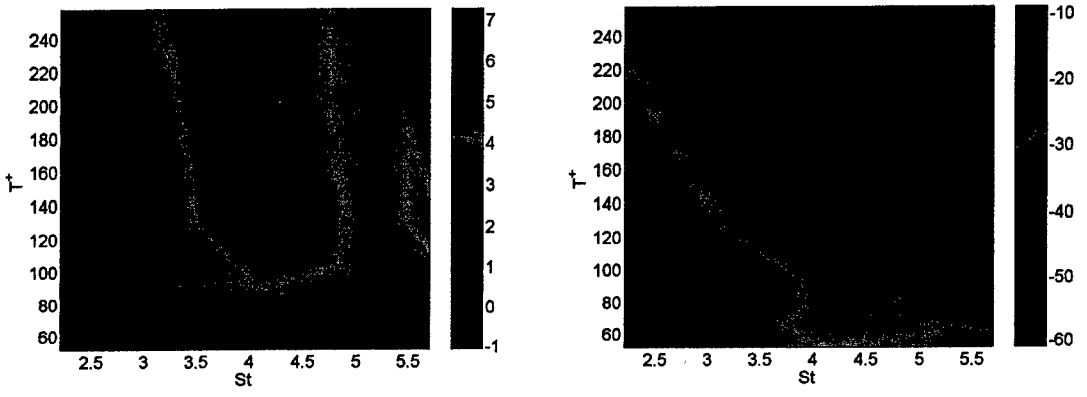

Figure 3.7: Percent change in flow rate and production terms over a wide range of forcing frequencies and amplitudes for a flow rate of $Re^* = 334$. The data shown represents five forcing frequencies and five forcing amplitudes.

the values of T^+ and St numbers presented here, and those which appear in the Breuer et al. [1] results. The difference is most likely a result of the calculation of the current density, J. In the current experiments, current was rigorously monitored for each case and the recorded number used directly in calculations. The current density in the previous experiments was most likely derived from the forcing amplitude, and thus was not as accurate.

3.2.3 Phase Synchronization

A separate experiment was run to determine the effects, if any, of the different phases of the forcing cycle on the mean flow and turbulence production. As mentioned in the experimental procedure, a sinusoidal wave was generated and amplified to drive the actuators. Data was taken at 90°, 180°, 270°, and 360°and plotted in comparison to the baseline. Figure 3.9 shows the mean profiles and the Reynolds stress for the actuated case chosen ($T^+St/Re^* = 4.7$). At the time the in-phase measurements were taken, the 'sweet spot' of actuation had not yet been determined, and thus a high voltage, low frequency case was chosen at random. The Reynolds stress and therefore the production for some phases go negative, which was not observed in any previous data. The variation between the cases is similar to that seen between baseline cases through the course of one experiment. The source of the negative values could possibly be attributed to experimental error; the experiments are inconclusive and will be run again to find a definitive explanation.

3.3 Second Order Statistics

3.3.1 Two-point correlations

Correlation coefficients were computed for each of actuated cases run. The correlation coefficient is defined as

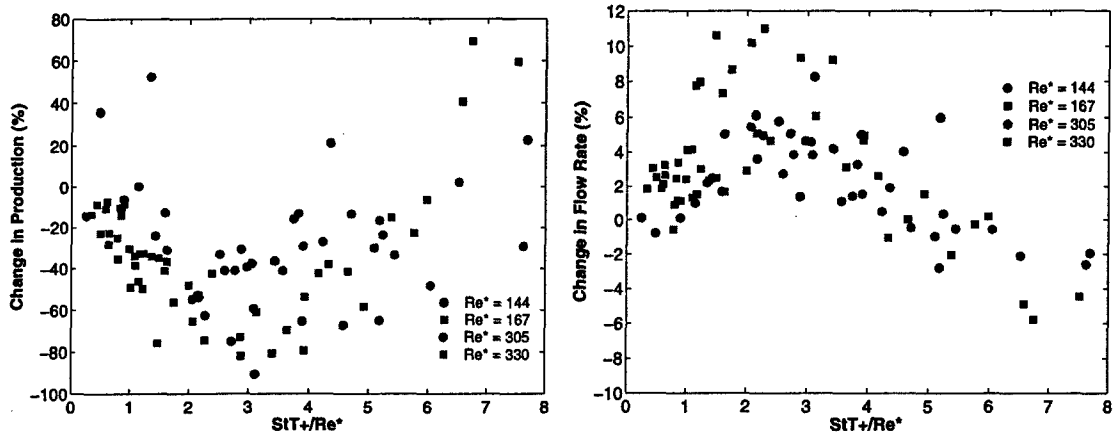

Figure 3.8: Changes in the turbulence production and flow rate as functions of the scaling parameter, StT^+/Re^*. Data from four different Reynolds numbers are shown and a wide range of forcing amplitudes and frequencies. Data collapses well, showing a minimum in production and maximum in flow rate at T^+St/Re^* between 2 and 3.

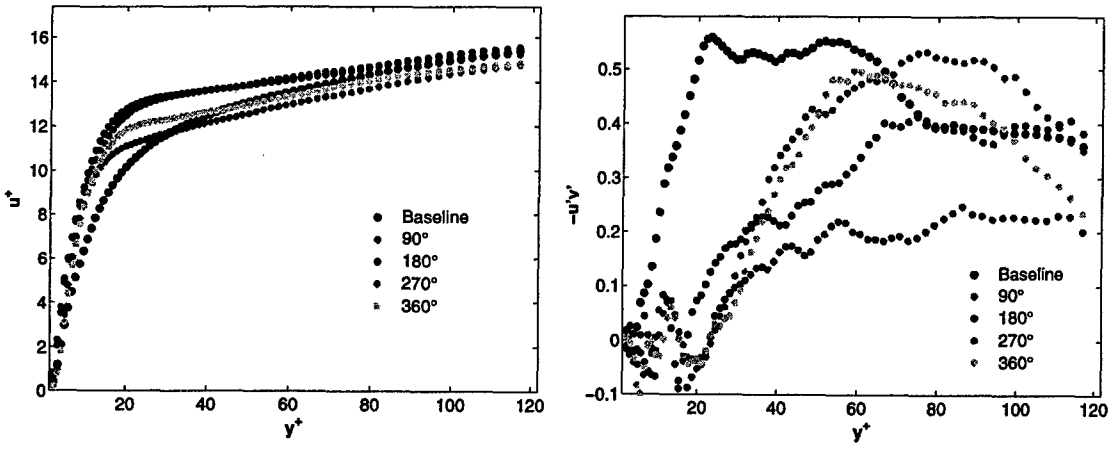

Figure 3.9: Mean and Reynolds Shear Stress taken at four different phases of the forcing cycle for a $Re^* = 200$.

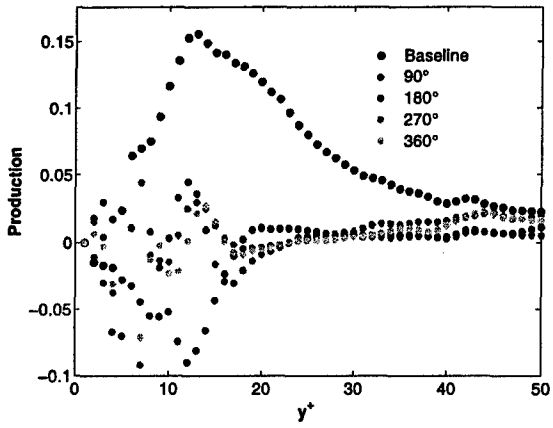

Figure 3.10: Turbulence production calculated for different phases of the forcing cycle.

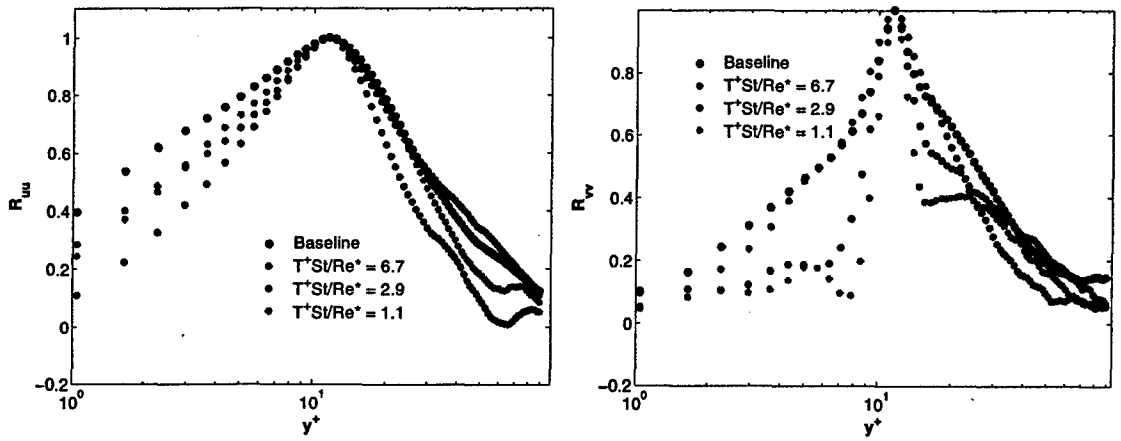

Figure 3.11: $R_{uu}(y_1, y_2)$ and $R_{vv}(y_1, y_2)$ at the location of maximum turbulence production, $y^+ = 12$. In all actuated cases, the correlation decreases, with a sweet spot at approximately $StT^+/Re^* = 2.9$

$$R_{ab}(y_1, y_2) = \frac{< a(y_1) \cdot b(y_2) >}{\sqrt{\overline{a^2(y_1)}} \cdot \sqrt{\overline{b^2(y_2)}}} \tag{3.2}$$

R_{uu}, R_{vv}, and R_{uv} were calculated for no control as well as all actuated cases at specific values of y^+. Figure 3.11 shows R_{uu} and R_{vv} at the location of maximum turbulence production for the lower velocity flow ($Re^* = 167$). All actuated cases show a lower correlation than the baseline case (blue circles). The greatest change comes in the near wall region, due to interaction with coherent structures. In this region, the T^+St/Re^* that produced the greatest increase in flow rate and decrease in turbulence production ($T^+St/Re^* = 2.9$) also represents the greatest decrease in correlation. In the R_{vv} correlation, the actuated cases also show a deviation from the baseline. The lowest frequency (red circles, $T^+St/Re^* = 6.7$) shows the least impact on the flow, while the higher frequencies show approximately the same reduction in correlation. A lower correlation of R_{uu} implies either smaller coherent

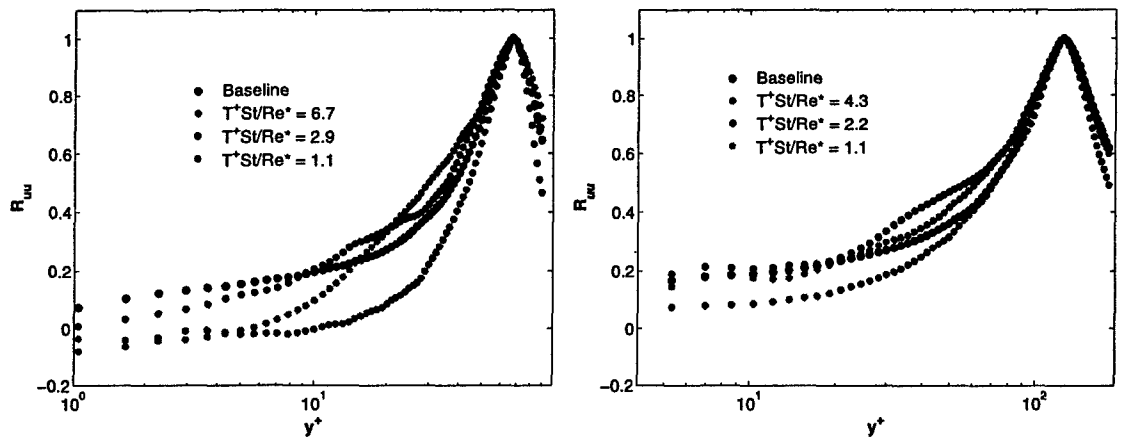

Figure 3.12: $R_{uu}(y_1, y_2)$ in the log layer for (a) $Re^* = 167$ at $y^+ = 76$ and (b) $Re^* = 330$ at $y^+ = 122$.

structures, fewer structures, or less coherence in the structure. It is inferred that the near wall disturbances created by the Lorentz forcing cause the lowest correlation to occur when $y^+ < 10$, as it is in this region that the forcing has the greatest impact. Figure 3.12 shows the correlations calculated for locations in the log layer for both the low and high Reynolds number flows. The effect of the forcing on the correlation decreases with distance from the wall as expected, given the penetration depth, $\Delta^+ \approx 9$ for the lower Reynolds flow.

3.3.2 Conditional Averaging

Based on the work of Johansson et al. [18] probabilities for the Reynolds shear stress were calculated. For each acquisition, the u' and v' were determined by subtracting the mean flow from the non-averaged total flow. Using these values, an instantaneous value of $-u'v'$ was determined. Dividing this instantaneous value by the averaged value, $-\overline{u'v'}$, gave an indicator of turbulent events. This probability, P, is plotted against the threshold value k in figure 3.13 for both high and low Reynolds flow. The baseline case is again represented with blue circles, with the other colors representing a frequency sweep at a constant amplitude. For the low Reynolds flow (left figure) the number of high intensity events decreases at optimum forcing (black circles), as expected. The high frequency case (red circles) which previously showed a decrease in flow rate and an increase in turbulence production, here demonstrates an increase in turbulence intensity events. In the case of the high Reynolds number flow, the actuated cases show no difference from the baseline for a threshold parameter k less than three. For values greater than three all actuated cases produce a greater number of high intensity events, which was not the expected result. It is proposed that with a greater St number (forcing voltage), a greater difference in the number of high intensity events will be observed. Further analysis will be conducted for a greater understanding of these results.

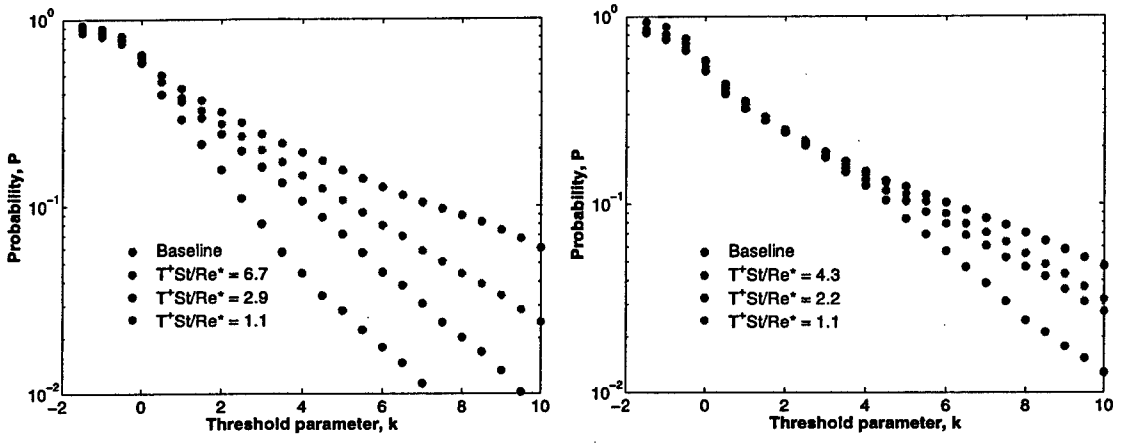

Figure 3.13: Probabilities plotted as a function of the threshold parameter, k, for a frequency sweep at a constant forcing amplitude for both low and high Reynolds number flow.

Chapter 4

Conclusions

Lorentz force actuators were tested in low Reynolds number saltwater channel flow to study the effects of near wall fluid perturbations. Robust actuators were designed, fabricated and tested and mounted in the Brown University flow facility. Particle Image Velocimetry was used to produce flow profiles for the mean flow as well as fluctuations for baseline and actuated cases. A range of forcing frequencies and amplitudes were tested based on the optimum forcing predicted by the dimensionless parameter T^+St/Re^* through two different Reynolds number ranges. From the mean flow profiles, a local flow rate was determined and found to increase greatly with the optimal forcing. Similarly, for optimum forcing parameters, the turbulence production was calculated and was found to decrease significantly with Lorentz force control. Control was greater with the lower Reynolds number flow, as predicted, as experimental constraints prevented scaling the T^+ and St numbers properly with the increase in Re^* number. Both the local flow rate and turbulence production were integrated over the entire range of scaling parameters, and broad areas of both positive and negative control were seen. The percent change from the baseline for both flow rate and production was plotted as a function of the dimensionless parameter T^+St/Re^*, and the optimal forcing was seen at $T^+St/Re^* \approx 2-3$. The experimental data taken in phase with the sinusoidal forcing proved to be inconclusive, and further experiments are needed to draw any definitive conclusions. Two point correlations were computed for all of the actuated cases, inferring a reduction in the size of the near wall coherent structures with Lorentz forcing. Conditional sampling was performed and low Reynolds number results were in agreement with the actuated data and correlation findings. Future research will include taking data in the $x-z$ plane to study the near wall structures, repeating the phase-locked forcing data, and further analyzing the conditional averaging data. Separation control using the Lorentz force has been proposed, and will hopefully be investigated in the near future.

Bibliography

[1] K. S. Breuer, J. Park, and C. Henoch. Actuation and control of a turbulent channel flow using Lorentz forces. *Phys. Fluids*, 16(4):897–907, 2004.

[2] R. D. Moser, J. Kim, and N. N. Mansour. DNS of turbulent channel flow up to $Re_{tau} = 590$. *Phys. Fluids*, 11:943–945, 1999.

[3] T. R. Bewley. Flow control: New challenges for a new renaissance. *Progress in Aerospace Sciences*, 37:21–58, 2001.

[4] H. Choi, P. Moin, and J. Kim. Active turbulence control for drag reduction in wall-bounded flows. *J. Fluid Mech.*, Vol. 262:75–110, 1994.

[5] W. J. Jung, N. Mangiavacchi, and R. Akhavan. Suppression of turbulence in wall-bounded flows by high frequency oscillations. *Phys. Fluids*, 4:1605–1607, 1992.

[6] H. W. Liepmann and D. M. Nosenchuck. Active control of laminar-turbulent transition. *J. Fluid Mech.*, 118:201–204, 1982.

[7] A. Seifert, S. Eliahu, D. Greenblatt, and I. Wygnanski. Use of piezoelectric actuators for airfoil separation control (TN). *AIAA J.*, 36(8):1535–1537, 1998.

[8] A. Seifert and L. G. Pack. Oscillatory control of separation at high reynolds numbers. *AIAA J.*, 37(9):1062–1071, 1999.

[9] Ari Glezer and Michael Amitay. Synthetic jets. *Ann. Rev. of Fluid Mech.*, 34:503–529, 2002.

[10] K. S. Breuer, J. H. Haritonidis, and M. T. Landahl. The control of localized disturbances in a boundary layer through active wall motion. *Phys. Fluids*, 3(1):574–582, 1989.

[11] T. C. Corke and E. Matlis. Plasma phased arrays for unsteady flow control. *AIAA Paper 2000-2323*, 2000.

[12] Kwing-So Choi, J-R. DeBisschop, and B. R. Clayton. Turbulent boundary layer control by means of spanwise wall oscillation. *AIAA Journal*, 36(7):1157, 1998.

[13] G. M. DiCicca, G. Iuso, P. G. Spazzini, and M. Onorato. Particle image velocimetry investigation of a turbulent boundary layer manipulated by spanwise wall oscillations. *J. Fluid Mech.*, 467:41–56, 2002.

[14] Junguo Pang and Kwing-So Choi. Turbulent drag reduction by Lorentz force oscillation. *Phys. Fluids*, 16:L35–L38, 2004.

[15] C. Henoch and J. Stace. Experimental investigation of a salt water turbulent boundary layer modified by an applied streamwise magnetohydrodynamic body force. *Phys. Fluids*, 7:1371, 1995.

[16] T. Berger, C. Lee, J. Kim, and J. Lim. Turbulent boundary layer control utilizing the Lorentz force. *Phys. Fluids*, 12:631, 2000.

[17] Y. Du and George Em Karniadakis. Suppressing wall turbulence by means of a transverse traveling wave. *Science*, 288:1230–1234, 2000.

[18] A. V. Johansson, P. H. Alfredsson, and J. Kim. Evolution and dynamics of shear layer structure in near wall turbulence. *J. Fluid Mech.*, 224:579–599, 1991.